ACS APPLIED NANO MATERIALS

www.acsanm.org Article

Wet-Chemical Synthesis of Porous Multifaceted Platinum Nanoparticles for Oxygen Reduction and Methanol Oxidation Reactions

Mario Daka, Marcello Ferrara, Manuela Bevilacqua, Paolo Pengo, Piu Rajak, Regina Ciancio, Tiziano Montini, Lucia Pasquato, and Paolo Fornasiero*

Cite This: *ACS Appl. Nano Mater.* 2022, 5, 4710−4720 Read Online

ACCESS | Metrics & More | Article Recommendations | Supporting Information

ABSTRACT: Herein, we report a facile and flexible synthesis of porous and highly faceted platinum nanoparticles (NPs) performed in the liquid phase. The synthesis is performed by reduction of platinum 2,4-pentantedionate in the presence of oleylamine and oleic acid in dibenzyl ether at 200 °C. The growth process was monitored by time-course transmission electron microscopy (TEM), revealing a peculiar progressive evolution that, in comparison with previous methodologies, is quite unusual. In fact, the morphology evolves first through nanocubes, nanostars, and dendrites to arrive at porous multifaceted NPs. This offers the possibility to selectively obtain materials with different degrees of complexity at a different time of reaction with one synthetic approach. Moreover, fine tuning of the reaction conditions was achieved by assessing, in dedicated experiments, the effects of temperature, surfactant concentration, and surfactant ratio, allowing control on NPs' dispersity and shape reproducibility. The dimensionally monodispersed NPs have a mean diameter of 52 ± 2 nm and display small regular crystallites with uniform facets exposed on the surface as evinced by high-resolution-TEM analysis. The as-prepared multifaceted platinum NPs were tested for oxygen reduction and methanol oxidation reactions exhibiting improved catalytic activity with respect to conventional Pt-based nanomaterials.

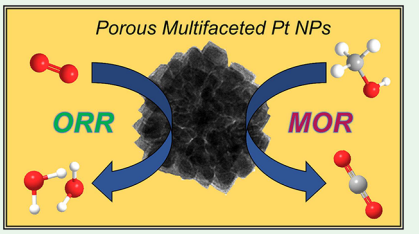

KEYWORDS: *porous nanostructures, platinum, controlled growth, faceted surface, ORR, MOR*

1. INTRODUCTION

Transition metal nanoparticles (NPs) have emerged during the past decades, displaying manifold potential applications in different fields such as catalysis,[1,2] nanomedicine,[3,4] and sensing.[5−7] Among all, platinum is of great interest and widely used because of its properties, such as high corrosion resistance and excellent hydrogen and oxygen adsorption capacity,[8] exploited mainly in homogeneous and heterogeneous catalysis;[9−16] therefore, much effort has been dedicated to the preparation of improved platinum-based NPs. It is well established that platinum NPs activity, as well as all metal-based nanomaterial activity, is mainly attributed to the composition,[17] large surface area,[18] and abundance of low coordination number sites.[19] In addition, defects (i.e., vacancies)[20,21] and the nature of crystallographic planes[22−25] also affect the activity of heterogeneous catalysts. Therefore, protocols aiming at obtaining platinum NPs with morphology control and size restraint should be preferred since they provide nanocrystals with promising catalytic properties. The development of methodologies for structural control over size and morphology aiming at enhancing selectivity and activity in tunable NPs[26] has also prompted interest toward metal nanomaterials in general, especially in the catalysis field.

Porous/dendritic platinum NPs, despite the lack of size confinement, have emerged in the material science and chemistry fields with applications in catalysis for the activation of small molecules.[27,28] The porosity of these NPs[29] can offer great advantages as pores and channels can host a great number of proximal active sites and enhance reactant diffusion, increasing the overall catalytic performances compared to non-porous NPs with the same dimensions.[30] In addition, the large surface area makes them approximable to aggregates of small NPs but with increased stability[31] and limited leaching and sintering issues.[32] Commonly, porous platinum nanostructures, prepared by wet-chemical methods, are synthesized by various approaches such as hard templating[33−35] and soft templating techniques,[36−39] de-alloying processes,[40,41] and electrochemical procedures.[42−44] Among all, preparation of porous platinum NPs by chemical reduction in the presence of soft templating agents is more convenient with respect to others because of its facile scalability and cost-effectiveness. In this context, various templates have been employed in the design of porous/dendritic NPs such as lyotropic liquids,[36] surfac-

Received: December 2, 2021
Accepted: March 23, 2022
Published: April 1, 2022

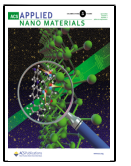

https://doi.org/10.1021/acsanm.1c04149
ACS Appl. Nano Mater. 2022, 5, 4710−4720

tants,[45,46] and polymers,[37] producing a variety of protocols that have contributed to the increased interest and availability of these metal NPs. Moreover, fine tuning of the reaction conditions opens the possibility of introducing unique features in the porous NP scaffold.[44,47,48] However, despite the increasing number of reported studies on these metals NPs, aspects like morphology control over lattice planes exposed on the surface and size monodispersity still remain hard to address and are a matter of study.

Herein, we report the synthesis of dendritic multi-faceted platinum NPs enriched in regular planes decorating the surface. By resorting to transmission electron microscopy to monitor the reaction course, we provide evidence of the unprecedented growth process of these NPs. The NPs were produced by the thermolytic reduction of platinum(II) 2,4-pentanedionate in dibenzyl ether as a solvent in the presence of oleylamine (OLAM) and oleic acid (OLAC) as directing and templating agents working under an argon atmosphere, respectively. The platinum NPs were then anchored on a carbon support and subjected to an optimized cleaning treatment consisting of washing steps with alkaline solution of NaOH in methanol,[49] necessary to expose the surface[50] without compromising the original morphology/nanostructure. Platinum represents nowadays the benchmark material for important electrochemical reactions, in particular, in the field of fuel cells development, such as proton exchange membrane fuel cells and direct methanol fuel cells, involved in automotive and portable applications, respectively. In accordance with a large-scale sustainability perspective, a fundamental target is to design high-performance Pt-based electrocatalysts with the lowest Pt consumption. Otherwise, a limitation of the Pt loading on the electrode surface could be related to not negligible downsides, such as strong performance losses and reduced stability. A promising strategy to overcome these losses is represented by the design of nanostructured low-Pt-content electrocatalysts to optimize the electrode texture and consequently the electrochemically active surface area (ECSA). Here, the NPs were tested in electrocatalysis for the oxygen reduction reaction (ORR) and the methanol oxidation reaction (MOR) in acidic media as proof of concept of catalytic activity for future applications.

2. EXPERIMENTAL SECTION

2.1. Materials. Oleylamine technical grade 70% (OLAM), oleic acid technical grade 90% (OLAC), benzyl ether 98%, ethanol 99.8%, methanol 99.8%, isopropanol 99.9%, toluene 99.7%, acetone 99.5%, conc. $HClO_4$ 70%, H_2SO_4 99.999%, and Nafion 117 5% solution were purchased from Sigma-Aldrich. Platinum(II) 2,4-pentanedionate (49.6% Pt) was purchased from Chempur, and Vulcan XC72R was supplied from Cabot. The 20% Pt on the carbon used as the standard was bought from Alfa Aesar. Bi_2O_3 was provided by Carlo Erba, and GeO_2 was provided by Johnson, Matthey & Co. All electrochemical experiments were performed with Milli-Q water obtained by using a Direct-Q (Millipore) water purification system. All the glassware used for the synthesis and deposition process of porous platinum NPs were previously cleaned with aqua regia (HCl/HNO_3 = 3/1) and then rinsed with Milli-Q water.

2.2. Synthesis of Porous Dendritic Pt NPs. Pt NPs were prepared by a surfactant-assisted process inspired by a previous protocol used in our group.[15] In a typical synthetic procedure, a three-necked 25 mL round-bottom flask, equipped with a stirring bar and internal thermometer, was flame-dried under vacuum and then purged with argon. Subsequently, 20 mg of $Pt(acac)_2$ (0.05 mmol), 2 mL of OLAM 70% (6.43 mmol), 2 mL of OLAC (7.11 mmol), and 10 mL of benzyl ether were added under argon flow to the flask and stirred at 100 °C using an oil bath for 10 min to completely dissolve the platinum complex and remove water traces. The temperature was then increased at 200 °C (5 °C min^{-1}), the flask was sealed, and the argon flow was stopped to better control the temperature. The reaction mixture was left to stir at 400 rpm for 1 h. At reaction completion, the flask was cooled to room temperature, ethanol was added (15 mL), and NPs were precipitated by centrifugation at 5000 rpm for 6 min and washed with ethanol/*n*-hexane 3 times and centrifuged again. Finally, the product was redispersed in *n*-hexane.

2.3. Deposition of Pt NPs on Carbon (Vulcan). Pt on carbon was prepared by a deposition process in an organic solvent. Typically, 50 mg of Vulcan was dispersed in 50 mL of toluene and sonicated for 30 min, and then the dispersion was stirred vigorously. Afterward, 10 mg of Pt NPs in 10 mL of *n*-hexane was added dropwise under constant stirring, and the suspension was left to stir for an additional 3 h. The as-prepared Pt/C was centrifuged at 5000 rpm for 12 min and washed 3 times with methanol before drying in vacuum at 60 °C for 12 h.

For methanol/NaOH treatment,[49] the dried catalyst was suspended in methanol followed by 150 mg of NaOH addition. The suspension was sonicated for 20 min until complete NaOH dissolution, and then the catalyst was collected by centrifugation at 5000 rpm for 12 min and washed with acetone (this procedure was repeated 3 times). The last washing step was performed with bi-distilled water, and the catalyst was filtered before drying at 60 °C under vacuum for 12 h.

2.4. Preparation of Sintered Pt NPs. Sintered Pt NPs on Vulcan were prepared starting from NaOH-treated NPs. Twenty milligrams of NaOH-treated porous Pt NPs on Vulcan was transferred to a 30 mL quartz tube reactor connected to a H_2/Ar line. The catalyst was first purged with Ar at room temperature for 30 min and then heated at 400 °C (ramp: 5 °C min^{-1}) under 100 mL min^{-1} H_2/Ar (3% H_2) flow for 4 h.

2.5. Electrode Preparation. All the inks were prepared in a 3:1 H_2O:iPrOH mixture with the addition of 0.05% (v/v) Nafion 117 5% solution and a catalyst concentration of 5 mg mL^{-1}. The ink was drop-casted on a polished GC-RDE in 8 μL drops till a loading of 30 μg_{Pt} cm^{-2} was reached for every experiment and dried in air flow with an RDE rotation rate of 700 rpm.

2.6. Electrochemical Measurements. All electrochemical characterizations were carried out at room temperature on an Autolab 302N electrochemical workstation (Metrohm, Autolab) by using a standard three-electrode setup. A GC rotating disk electrode (RDE Metrohm, Autolab, geometric SA: 0.196 cm^2) was used as the working electrode. A Pt wire and a saturated calomel electrode (SCE, KCl sat.), counter and reference electrodes, respectively, were separated from the main chamber via bridges equipped with Vycor frits. According to the recent literature,[51] the use of Pt as a CE is strictly recommended to be avoided when the electrochemical study is referred to highlight the activity of non-precious metal-based catalysts, in particular, Pt-free electrocatalysts in acidic media and for prolonged measurements (HER and ORR chronoamperometric studies). In the present case, we investigated Pt-based materials. Furthermore, the Pt CE was carefully separated from the main cell chamber to further minimize interferences, as proven by a crosscheck comparison with a carbon-based CE. All the characterizations were done following the procedures reported by Shinozaki et al.[52,53] To completely clean the surface of the nanoparticles from any possible residue, 200 cycles of CV were used at 0.5 V s^{-1} between 0 and 1.2 V vs RHE. During this conditioning, the hydrogen adsorption and desorption peaks became more accentuated and symmetric until a stable response from the material was obtained. All electrocatalytic experiments were corrected for ohmic losses and background currents (i.e., capacitive currents). Two parameters were chosen to compare different catalytic results, specific activity (SA, mA cm_{Pt}^{-2}) and mass activity (MA, mA mg_{Pt}^{-1}), both measured at potentials of interest for the specific catalytic reaction.

In order to evaluate the ECSA of the platinum NPs, many different procedures can be found in the literature, resulting in high variability in ECSA values (even in orders of magnitude).[54] Here, we followed

https://doi.org/10.1021/acsanm.1c04149
ACS Appl. Nano Mater. 2022, 5, 4710−4720

Scheme 1. Representative Synthetic Scheme for the Porous Multifaceted Platinum Nanoparticles

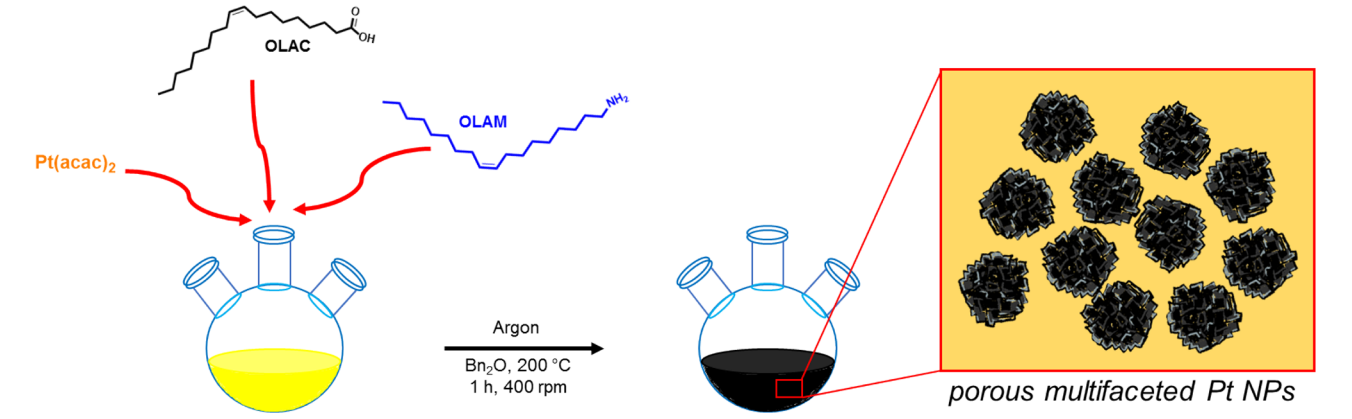

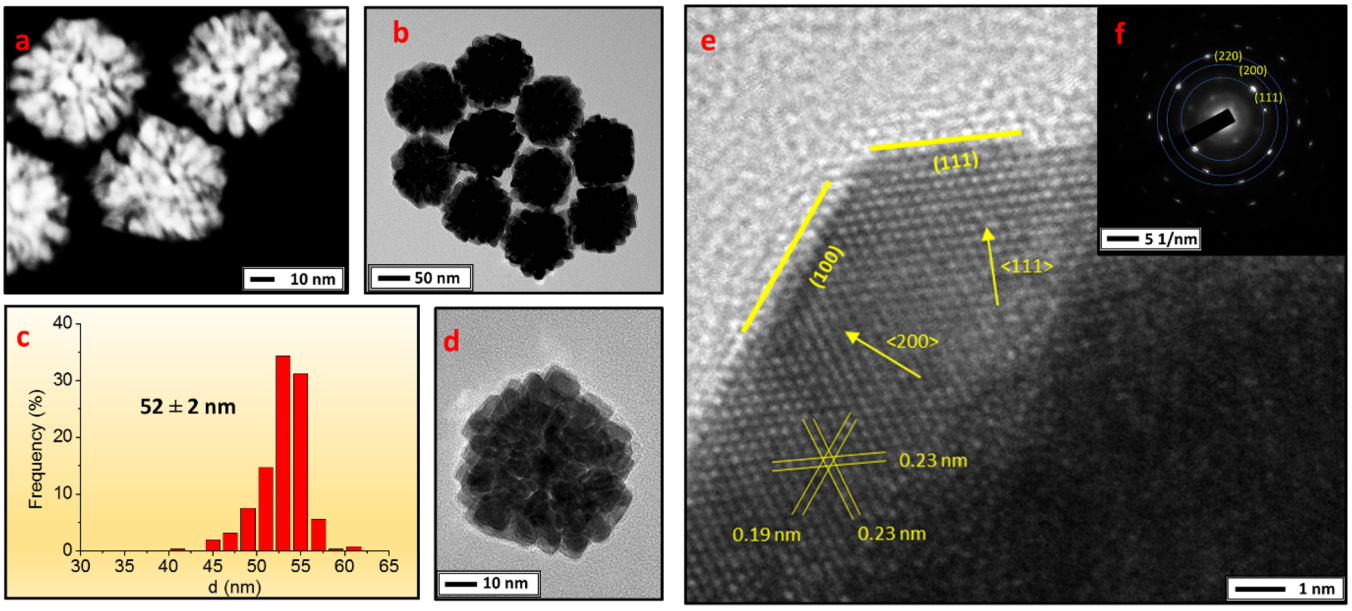

Figure 1. Representative HAADF-STEM image of the Pt NPs (a); low magnification (b), dimensional analysis (c), and high magnification (d) TEM images of the NPs; HR-TEM image of the Pt crystallite (e) and selected-area ED patterns (f).

the most straightforward procedure based on the integration of H_{upd} related peaks in the CV performed at 0.1 V s^{-1}. The ECSA was obtained by dividing the as obtained charge with the standard value of 210 μC cm^{-2}, normalized for the Pt NPs mass. Roughness factors (RF) were calculated as ECSA values times the material loading:

$$\text{ECSA} = \frac{Q_{\text{UPD}}\ (\mu\text{C})}{210\ \mu\text{C cm}^{-2}} \frac{1}{m_{\text{Pt}}}$$

$$\text{RF} = \text{ECSA} \times \frac{m_{\text{Pt}}}{\text{SA}_{\text{geo}}}$$

To better rationalize the presence of different symmetry sites on both unsupported Pt-NPs and Pt/C electrocatalysts, we investigated the irreversible surface adsorption of Ge and Bi as foreign adatoms.[55−57] The adsorption of bismuth was performed in an acidic saturated Bi_2O_3 (0.5 M H_2SO_4). After the adsorption of Bi on the electrode surface, the electrode was rinsed with ultra-pure water and immersed at 0.05 V in the three-electrode cell setup containing a 0.5 M H_2SO_4 electrolyte. The adsorption of Ge was performed in a solution containing GeO_2 (10^{-2} mol L^{-1}) and NaOH (1 mol L^{-1}). The working electrode was transferred to an electrochemical cell with H_2SO_4 (0.5 mol L^{-1}) and immersed at 0.10 V vs RHE. The positive sweep scans were recorded before and after the adsorption steps of Ge and Bi in the potential range of 0.05−0.80 V at 20 mVs^{-1}. To ensure the adequate cleanliness of the Pt/C electrode surface, we selected a specific protocol adopted by Aldaz and co-workers,[58] suitable for more complex systems than Pt well-defined single crystals.

2.7. Characterization. TEM analyses were performed using a Philips EM 208 microscope operating at 100 kV and equipped with an 11 MP bottom-mounted CCD Olympus Quemesa camera. High-resolution TEM (HR-TEM) images, selected-area electron diffraction (SAED) patterns, and high-angle annular dark field (HAADF) scanning TEM (STEM) were acquired by using a JEOL 2010 UHR field emission gun microscope operated at 200 kV with a measured spherical aberration coefficient Cs of 0.47 ± 0.01 mm. The electron dose rate was 1.5 × 10^{-8} e/sÅ^2 for regular and HR-TEM imaging. HAADF-STEM images were acquired using an illumination angle of 12 mrad and a collection angle of 88 ≤ 2θ ≤ 234 mrad. Textural properties were analyzed by N_2 physisorption at the liquid nitrogen temperature using a Micrometrics ASAP 2020 automatic analyzer. All the NPs were degassed at 50 °C for 12 h at 10 μmHg. The specific surface area was obtained by applying the Brunauer−Emmett−Teller (BET) method equation. Pore size distribution was determined applying the Barrett, Joyner, and Halenda (BJH) method equation to the desorption branch of the isotherms. H_2 chemisorption was performed using a Micrometrics ASAP 2020C apparatus. A chemisorption stoichiometry H:M = 1:1 was assumed for the calculation of the exposed metal surface area. The materials have

https://doi.org/10.1021/acsanm.1c04149
ACS Appl. Nano Mater. 2022, 5, 4710−4720

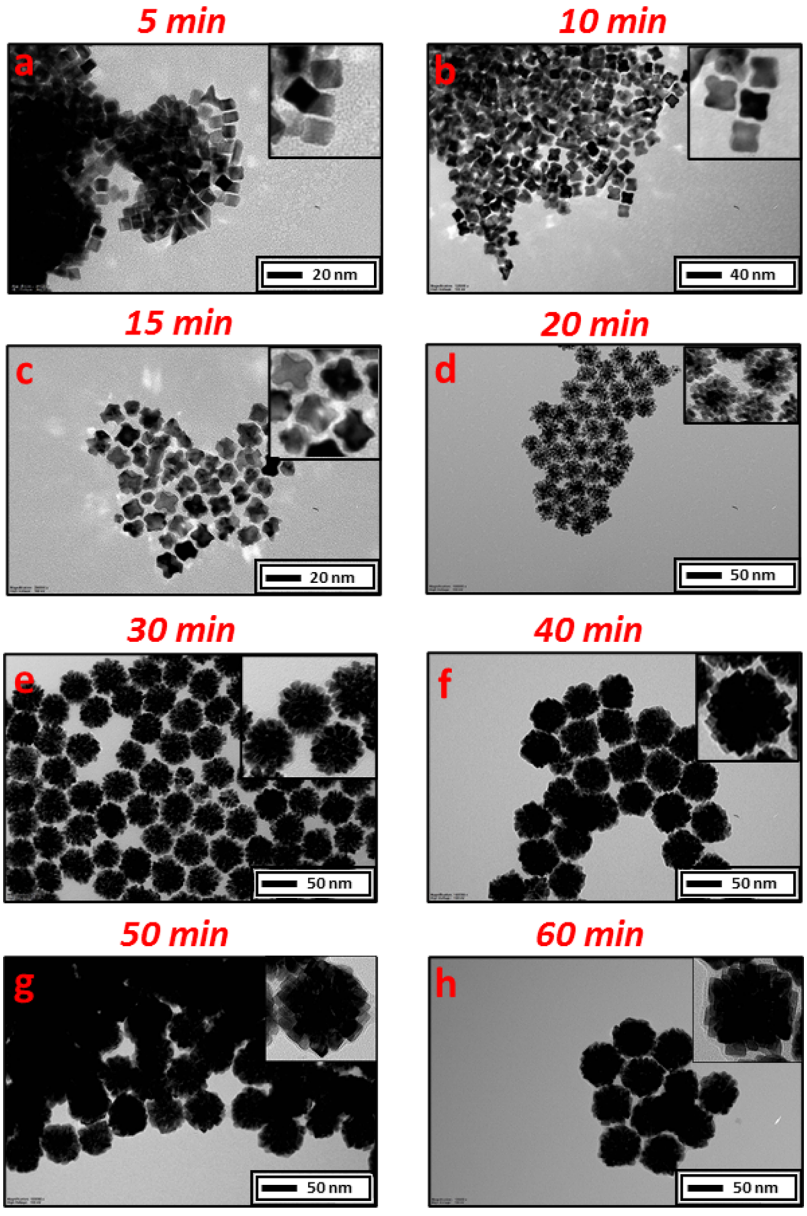

Figure 2. Typical TEM images representing the size and shape progression of the porous Pt NPs at 5 (a), 10 (b), 15 (c), 20 (d), 30 (e), 40 (f), 50 (g), and 60 min (h).

been degassed at 100 °C for 6 h. H_2 chemisorption isotherms have been recorded in a 1−400 Torr pressure range at room temperature. The Pt concentration in the catalyst was quantified by means of inductively coupled plasma-optical emission spectrometry (ICP-OES) using an Optima 8000 instrument (Perkin Elmer; Waltham, MA, USA) with an integrated S10 autosampler. A five-point standard curve was used for ICP-OES measurements (range: 0−10 mg L^{-1}). The limit of detection at an operative wavelength of 228.616 nm was 0.01 mg L^{-1}. Powder X-ray diffraction (XRD) analysis was performed on an X'Pert Philips MPD with monochromatic Cu Kα radiation (λ = 1.5406 Å), and the range used was 2θ = 10−120° in Bragg−Brentano geometry with a step size of 0.0263°. The average crystallite size was determined applying the Scherrer equation $D = (k \times \lambda)/(\beta\cos\theta)$ where D is the mean size of the crystallite, the Scherrer constant k = 0.9354 was obtained by tabulated values for the octahedral crystallites determined for hkl = 111, λ is the X-ray wavelength expressed in Å, β is the full width at half maximum of the first XRD peak expressed in radians, and θ is the Bragg angle. IR spectra were recorded in attenuated total reflectance (ATR) mode on a Shimadzu IRAffinity-1S spectrophotometer equipped with a QATR 10 accessory.

3. RESULTS AND DISCUSSION

3.1. Synthesis and Characterization of Porous Multifaceted Pt NPs. In this work, the synthesis of porous platinum NPs was performed by a wet-chemical procedure (Scheme 1) in dibenzyl ether, a high-boiling-point solvent, to easily reach the metal thermal reduction temperature (for platinum, ca. 200 °C).

Platinum 2,4-pentanedionate OLAM, OLAC, and the solvent were first purged in argon at 100 °C for 10 min to remove air and moisture that, at high temperatures, can generate violent bursts. Then, the temperature was increased up to 200 °C with a ramp of ca. 5 °C min^{-1} and maintained for 60 min.

A synoptic overview of the electron microscopy characterization for the obtained NPs is presented in Figure 1. HAADF-STEM and TEM images (Figure 1a,b, respectively) show that the obtained dendritic NPs have remarkably uniform shape and a narrow size distribution. Indeed, as shown in the particle

https://doi.org/10.1021/acsanm.1c04149
ACS Appl. Nano Mater. 2022, 5, 4710−4720

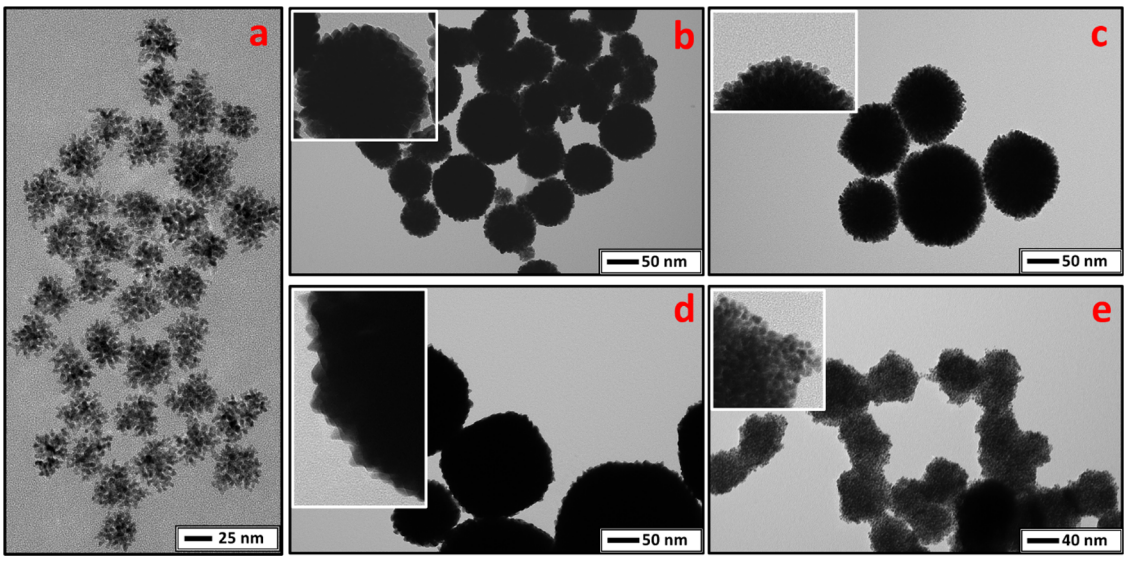

Figure 3. Representative TEM images of synthesis performed at 180 °C (a), 210 °C (b), 600 rpm (c), only OLAM as the surfactant (d), and only OLAC (e).

size distribution histogram (Figure 1c), a mean diameter of around 52 ± 2 nm for a set of ~400 particles is measured. The most notable aspect of these nano-objects is the regular edges that decorate their surface as observed in Figure 1b,d. The high-magnification micrograph of a single particle (Figure 1d) highlights the porous structure and abundant presence of shaped crystallites with an average dimension of 10 ± 1 nm (Figure S1). The crystallites are well oriented and hierarchically assembled to constitute the porous NPs themselves. The HR-TEM image of the crystallites unveils well-defined terraces composed of uniform low-indexed planes as evinced in Figure 1e. Although regular terraces dominate the surface of these NPs, defects and steps are also observed (Figure S2). In addition, from the SAED pattern (Figure 1f), the main diffraction rings of the first reflections of the Pt face-centered cubic (fcc) lattice (111), (200), and (220) planes can be identified. The well-defined bright spots on the diffraction ring patterns indicate the high crystallinity of the synthesized NPs. Surface area measurements were performed on the Pt NPs to support their potential application in catalysis. Nitrogen adsorption/desorption isotherms (Figure S3) measured at the liquid nitrogen temperature revealed a BET surface area of 15.4 m^2 g^{-1}, which is consistent with previously reported syntheses of porous Pt nanostructures in the organic phase.[59] The pore size distribution of the unsupported NPs (Figure S4) gave an average pore diameter of 35 nm that is much larger than the voids observed in the porous Pt NPs by TEM analyses. This result indicates that the major contribution to the pore volume in the dried sample is related to the voids formed by the aggregation of the porous Pt NPs, with the inner space between the aggregated crystallites being less important.

To further understand the NP morphology and the arising of faceted crystallites decorating the NP surface, the synthesis was monitored at an increasing reaction time by TEM analysis. The start of the temperature ramp from 100 to 200 °C was arbitrarily chosen as time zero, and small aliquots (0.2 mL) of the reaction mixture were withdrawn every 5 or 10 min and analyzed after a quick purification step (hexane/ethanol washing and centrifugation at 15,000 rpm). The electron dose rate and the image acquisition conditions were properly set to avoid unwanted beam effects. The growth process and morphology evolution of the Pt NPs are summarized in Figure 2. After 5 min of reaction time (Figure 2a), small cubic NPs with an average size of 8 ± 1 nm were observed. The nucleation stage of porous Pt nanostructures usually involves the formation of polycrystalline seeds or small dendrites[46,60,61] due to the fast kinetically controlled reduction of the platinum precursor. We observed this behavior when the addition of OLAM and OLAC was performed at 120 °C and with 5 min delay one from the other independently of the introduction order (Figure S5). In our procedure, however, the use of OLAM and OLAC (added simultaneously at room temperature), known for their ability to be adsorbed on specific facets, promotes the directional growth of NPs.[62] In addition, the absence of strong reducing agents, but the use of OLAM as a reducing agent,[63] can offer a thermodynamic control on the nucleation process by minimizing the surface energy, leading to the initial cubic-shaped NPs displayed in Figure 2a. While primary particles may still be produced after 5 min, we observed that this process is also accompanied by a morphology change of the already produced NPs. Indeed, at this stage, the $Pt(acac)_2$ reduction continues to take place, giving a preferential growth of the nanocubes along the ⟨111⟩ axes, as highlighted by the elongated vertexes of the cubes after 10 min (Figure 2b), eventually delivering star-shaped NPs after 15 min (Figure 2c). The TEM images of the sample collected at 20 min (Figure 2d) mark a change in the NP morphology, with the deposition of small polycrystalline clusters on the star-shaped NPs that quickly grow in elongated branches, giving rise to porous dendrites. This quick change in morphology can be related to the temperature that reaches 200 °C at this stage and remains steady for the rest of the process. At this temperature, the thermal platinum reduction is likely boosted, driving the NP growth toward a kinetic control and promoting the formation of polycrystalline nanostructures. From 30 to 40 min (Figure 2e,f), while there are no relevant changes in size (see Figure S6 for dimensional analysis) of the Pt dendrimers, thickening of their branches is clearly visible. This latter process gives rise to the formation of regular facets on the NP surface, and the overall NP morphology does not further

https://doi.org/10.1021/acsanm.1c04149
ACS Appl. Nano Mater. 2022, 5, 4710−4720

change at 50 or 60 min reaction times (Figure 2g,h). This latter behavior suggests a thermodynamic control driving the NP surface energy to its minimum. The time-course TEM analysis in the synthesis of porous faceted Pt NPs played a crucial role in studying the formation of present Pt NPs. As previously established, step-by-step TEM monitoring provides direct feedback useful in addressing the formation mechanisms dominating the different phases of the NP preparation.[64] In agreement to what was already documented for the growth mechanism of porous/dendritic Pt NPs, here, a continuous seed formation followed by a fast autocatalytic aggregation-based growth was observed.[59,65,66] Nevertheless, an additional benefit concerning the narrow size distribution of the nanoparticles was achieved. Monodispersity has been sporadically documented by previously reported synthetic methodologies for porous NPs,[67−69] while a common ill-defined size distribution is mainly reported.[46,66,70]

To investigate the robustness of the synthesis, control experiments were performed under conditions away from the optimum. While the effect of the precursor concentration was previously investigated, showing a correlation with size and morphology changes,[70,71] we focused on different aspects that still affect the synthesis such as the temperature, stirring rate, and ligand molar ratio. First, a control experiment in air confirmed the needful use of inert gas for the successful production of multifaceted porous NPs. In fact, in an air atmosphere, polycrystalline porous NPs were obtained (Figure S7). When the synthesis was performed at 180 °C for 1 h, a dark-yellow solution was obtained (Figure S8), delivering a very low quantity of smaller dendritic NPs as reported in Figure 3a. Although OLAM can act as a reducing agent for metal salts at lower temperatures,[72] in our procedure, the thermally boosted reduction at 200 °C is pivotal for the production of these NPs. On the other hand, the reaction performed at higher temperatures (210 °C) resulted in bigger and polydispersed NPs (Figure 3b), but terraces can still be detected on the surface (inset of Figure 3b). Increasing the stirring rate from 400 to 600 rpm is sufficient to modify the ideal conditions responsible for the minimization of surface energy and deliver polydispersed porous NPs without the shaped features (Figure 3c). The use of exclusively OLAM or OLAC as a surfactant resulted in large NPs with no distinct porosity (Figure 3d) but highly enriched in regular vertexes (inset of Figure 3d) and in densely packed aggregates of small crystallites (Figure 3e and inset), respectively. Moreover, screening of different OLAM/OLAC molar ratios (1/3, 1/1.5, 1.5/1, and 3/1) resulted in porous but dimensionally polydispersed NPs (Figures S9 and S10), except OLAM/OLAC = 1/3 that delivered small crystallites (Figure S9a) like those produced using only OLAC as the surfactant. Surprisingly, NPs obtained by different OLAM/OLAC molar ratios do not display the shape uniformity and the facets achieved under the optimized conditions. By plotting the concentration variation of [OLAM]/[OLAM + OLAC] versus the NP dimension, a monotonic upward trend is observed that correlates the higher OLAM concentration to the increasing NP dimension (Figure S11). Considering these aspects, we can speculate a synergistic effect of OLAM and OLAC, when used at the same molarity, in creating the right environment for the formation of uniform and monodisperse porous multifaceted Pt NPs. Moreover, by fine tuning the reaction conditions, it is possible to obtain batches of homogeneous materials with different sizes and shapes and potential different properties.

3.2. Textural Properties. The synthesized porous Pt NPs were deposited on a Vulcan XC72R support to obtain suitable materials for electrocatalytic studies. The composite material and a commercial Pt/C material used as the reference have been characterized to relate their properties with the electrochemical performances. Notably, the composite porous Pt NPs/Vulcan material was prepared with a metal loading of 15 wt %, as determined by ICP-OES analysis. This value is comparable with the nominal 20 wt % reported for the commercial Pt/C reference material.

Textural properties of the composite porous Pt NPs/Vulcan and the commercial Pt/C materials are very similar (Figures S12 and S13 and Table S1), with a high surface area and pore volume and an extended mesoporous network around 63 nm. The most relevant differences between these two samples are a slightly larger contribution of micropores, a relative maximum centered around 3.6 nm in the mesopore size distribution, and a significantly lower cumulative pore volume for the commercial Pt/C material. As expected, the pristine Vulcan XC72R shows a higher surface area and pore volume than the composite porous Pt NPs/Vulcan material, considering the higher density of Pt with respect to the carbon support. Notably, after sintering of the composite porous Pt NPs/Vulcan under H_2 at 400 °C, no significant modifications of the textural properties are observed.

H_2 chemisorption experiments have been performed on the various Pt/C materials to analyze the Pt-exposed surface area. H_2 chemisorption isotherms are presented in Figure S14, and the obtained results are summarized in Table S2. The composite porous Pt NPs/Vulcan chemisorbed a remarkably lower amount of H_2 with respect to the commercial Pt/C material. As a consequence, metal dispersion and exposed surface areas (reported irrespectively of the mass of the catalyst or to the mass of Pt) are lower, and the apparent metal particle size is larger for the composite porous Pt/Vulcan material. It is straightforward to note that, in the composite porous Pt/Vulcan material, the exposed metal surface area reported with respect to the mass of Pt is 18.1 $m^2\ g_{Pt}^{-1}$, which is very close to the value of 15.4 $m^2\ g^{-1}$ measured by N_2 physisorption on the pristine porous Pt NPs, even considering the intrinsic systematic errors of the two different techniques. Moreover, powder XRD analysis of the composite porous Pt/Vulcan material (Figure S15) showed the typical reflection of metal Pt (JCPDS 04-0802), together with a very broad reflection around 26° due to the crystalline graphitic portion of Vulcan XC72R. The peak broadening of the (111) reflection of Pt is compatible with an average crystallite size of 11 nm, the same measured for the pristine porous Pt NPs. This result suggests that the porous nature of the Pt NPs is preserved during the various steps involved in the preparation of the composite porous Pt NPs/Vulcan (deposition protected porous Pt NPs and washing removed organic ligands). Notably, after the sintering treatment in H_2 at 400 °C, the exposed metal surface area drastically decreased, confirming the deep sintering on the Pt nanoparticles.

Furthermore, the morphology of the various Pt/C samples was analyzed by TEM. A representative TEM image of the commercial Pt/C sample (Figure S16) shows the presence of highly dispersed Pt nanoparticles, with a mean diameter of 3−4 nm. On the other hand, TEM images of the composite porous Pt/Vulcan material (Figure S17) shows the presence of the porous Pt NPs deposited on the carbonaceous support: despite the limited contrast due to the thickness of the support around

https://doi.org/10.1021/acsanm.1c04149
ACS Appl. Nano Mater. 2022, 5, 4710−4720

the porous Pt NPs, the aggregation of various Pt crystallites to form a porous particle is clearly visible. After sintering by H_2 treatment at 400 °C, TEM analysis (Figure S18) confirms the coalescence of the Pt crystallite to form very large metal particles with spherical shapes. All the results obtained by TEM analysis of the supported Pt/C materials, investigated in electrocatalytic tests, are fully in agreement with the H_2 chemisorption results.

3.3. Electrocatalytic Investigations. The standard thermal cleaning procedure could not be applied to the present nanostructure Pt-based systems as they would be subjected to structural and morphological modifications. After electrode conditioning, all samples were therefore subjected to cyclic voltammetries (CVs) at 0.1 V s^{-1} to clean and investigate the surface of the catalyst. Commonly, platinum-based materials CVs can be divided into three areas accounting for different contributions: the hydrogen region, the double layer (DL) region, and the oxide region.[73] The characteristic CVs for the three materials tested are reported in Figure 4. The

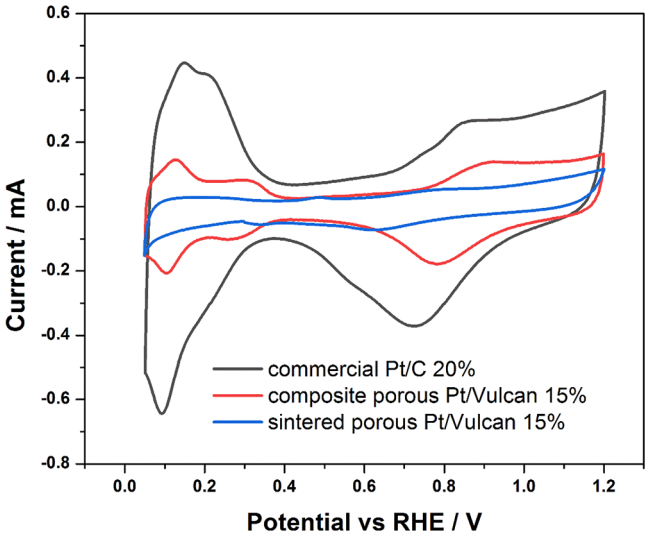

Figure 4. CVs of commercial Pt/C (black), composite porous Pt/Vulcan material (red), and sintered porous Pt/Vulcan material (blue) registered at 100 mV s^{-1} in $HClO_4$ 0.1 M.

DL region (0.4−0.6 V vs RHE) is mainly influenced by the carbon support: from the lower capacitive currents, we can infer that the Vulcan XC72R has less surface area accessible to the ions in solution than the carbon used in the commercial Pt/C. In the hydrogen region, the CV peaks can reveal the features of the exposed platinum surfaces. The commercial Pt/C material shows two close peaks at 0.15 and 0.2 V vs RHE: while the first can be related to (110) step sites, the origin of the second peak is somewhat still debated and could arise from (111) sites.[74] Similarly, the composite porous Pt/Vulcan shows a peak at 0.13 V and one at 0.3 V vs RHE, with (110) and (100) step sites also present on the surface.[74] The selective adsorption measurement of foreign adatoms, such as Ge and Bi, was used to investigate well-defined single-crystal electrodes,[55−57] thin films,[75] and, in a few cases, more complex Pt nanoparticles.[57] Notably, the resulting voltammetric profile of the materials after the metal deposition is strongly affected by the initial cleanliness of the electrode surface (usually performed by means of electrode annealing). The higher complexity of the unsupported Pt-NPs and Pt-NPs/C systems investigated in the present work with respect to the bare Pt crystals previously investigated[55−57] originates from the poly-oriented nature of the NPs and from the presence of the carbon support (Vulcan) for the composite electrocatalyst. The resulting broad and multipeak features, characterizing the voltammetric scans after Ge and Bi adsorption (see Figures S19 and S20), suggest the presence of different surface sites in addition to the (100) and (111), already detected by HR-TEM (Figure 1e), even if major contributions from trace impurities in the used reagents cannot be fully excluded.

From the area of the H desorption peaks, ECSAs and RFs can be calculated for the three samples. As expected, the commercial Pt/C material shows the highest electrochemical surface areas due to the very low dimensions of the Pt nanoparticles. The ECSA for the composite porous Pt NPs/Vulcan is one-half than that of the commercial reference material. After sintering, only 25% of ECSA is retained (Table 1). These results are in good agreement with the trend

Table 1. ECSAs and RFs of the Investigated Catalysts

	ECSA (m^2 g^{-1})	RF
commercial Pt/C	6.3	1.9
composite porous Pt NPs/Vulcan	2.9	0.87
sintered porous Pt NPs/Vulcan	0.71	0.21

observed for the exposed metal surface area measured by H_2 chemisorption. The large difference between the values of metal surface area from electrochemical measurements and H_2 chemisorption can be clearly related to the differences in the techniques: H_2 chemisorption counts for all the exposed surface Pt atoms, while the ECSA takes into account only the atoms that can be reached by diffusion of electrons in the overall assembly of the electrode. Moreover, the cathodic and anodic sweeps of the composite porous Pt NPs/Vulcan material show very good symmetry in the hydrogen region. This indicates high reversibility of the phenomena due to the clean surface that was confirmed by IR analysis of the pre- and post-treated catalyst with NaOH (Figure S21).[53]

3.3.1. Oxygen Reduction Reaction (ORR). ORR catalytic activities of the different Pt-C composites were investigated via linear sweep voltammetry (LSV) in acidic electrolyte (0.1 M $HClO_4$) saturated with pure O_2 from 0.1 to 1.1 V vs RHE at a scan rate of 10 mV s^{-1} (Figure 6). Catalyst loading varied for the different materials between 153 (for commercial Pt/C) and 187 μg cm^{-2} (for composite porous and sintered Pt NPs/Vulcan), corresponding to a fixed loading of ~30 μg_{Pt} cm^{-2}. The LSV results obtained for ORR in $HClO_4$ 0.1 M for the investigated materials are presented in Figure 5, while Figure 6 summarizes the MAs, normalized with respect to the mass of Pt, and SAs, normalized with respect to the ECSA of each material. The comparison of the obtained results highlights the importance of porosity of the Pt NPs in our material. The sweeps of commercial Pt/C and composite porous Pt NPs/Vulcan are very similar, showing higher activities per unit area for the porous nanoparticles. The composite porous Pt NPs/Vulcan shows comparable MA with respect to the commercial Pt/C material, but, having a lower ECSA, its SA is much higher than that of the reference material. Overall, the material displays higher MA and SA for ORR, compared to other porous or non-porous Pt-based nanomaterials from the literature.[41,76] At the same time, the sintered Pt NPs/Vulcan shows a very low MA, while the SA is closer to that of the

https://doi.org/10.1021/acsanm.1c04149
ACS Appl. Nano Mater. 2022, 5, 4710−4720

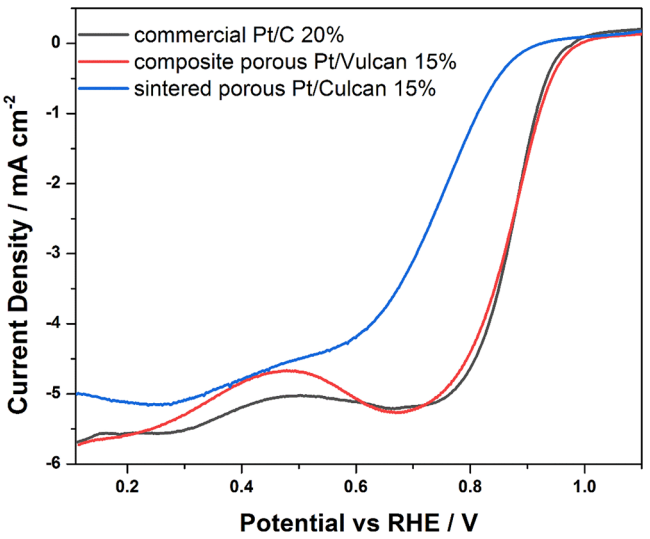

Figure 5. LSVs for commercial Pt/C (black), composite porous Pt/Vulcan material (red), and sintered porous Pt/Vulcan material (blue) registered at 10 mV s^{-1} from 0.1 to 1.1 V in 0.1 M $HClO_4$ solution at 1600 rpm. Visualized potentials are corrected for pH and ohmic losses.

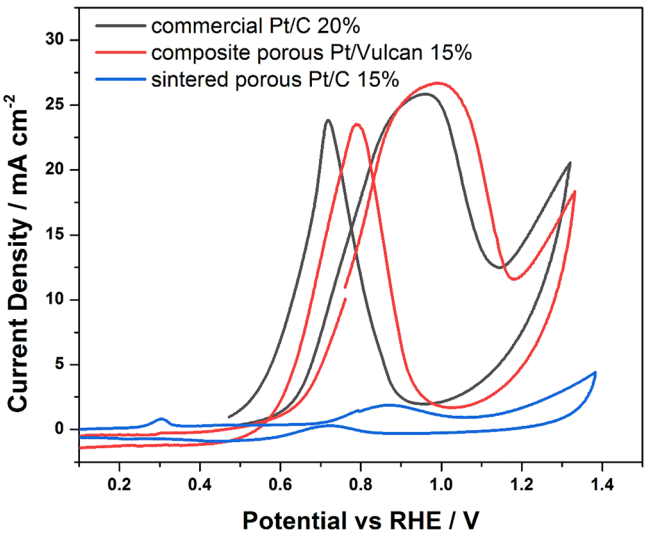

Figure 7. CVs of commercial Pt/C (black), composite porous Pt/Vulcan material (red), and sintered porous Pt/Vulcan material (blue) registered at 50 mV s^{-1} in a 10% vol MeOH sol. in 0.1 M $HClO_4$ from 0.1 to 1.5 V. Visualized potentials are corrected for pH and ohmic losses.

reference commercial Pt/C. The peculiar performance of the composite porous Pt NPs/Vulcan expressed in terms of SA could arise from the well-defined morphology of the Pt crystallites.

3.3.2. Methanol Oxidation Reaction (MOR). MOR catalytic activities of the different Pt/C composites were investigated via CV in an acidic electrolyte (MeOH 10 vol % in 0.1 M $HClO_4$) in Ar between 0.4 and 1.4 V vs RHE at a scan rate of 50 mV s^{-1} (Figure 7), while normalized activities (MA and SA) are presented in Figure 8. The platinum loading was fixed at ~30 μg_{Pt} cm^{-2}. The MOR behavior of the three materials is similar to the case of ORR. Specific activities calculated on the forward scan for the non-porous materials (commercial Pt/C and composite sintered Pt/Vulcan) are comparable, while the porous nature and exposed facets in the composite porous Pt/Vulcan sample result in better performance of the electrocatalyst. Again, mass activities do not show a significant difference between the commercial Pt/C and composite porous Pt/Vulcan, pointing to a balancing effect between the lower ECSA and higher specific activity. Due to different ways of setting up the MOR experiments, it is difficult to compare results with the literature. Where a comparison is possible, our material displays higher mass and specific activities toward MOR with respect to other porous and non-porous Pt-based nanomaterials.[34,46,77]

4. CONCLUSIONS

A straightforward and rapid synthesis was developed for the preparation of porous multifaceted Pt NPs. The reaction was performed in the presence of OLAM and OLAC that showed to be crucial to achieve the complex architecture of the NPs. Reduction of the precursor was promoted by the high temperature and the presence of OLAM, without the use of a strong reducing agent. The as-prepared NPs were very uniform in shape and strikingly monodisperse with a good grade of porosity. The growth mechanism displayed an unusual morphological transition of the NP shape never observed before. Finally, the resultant NPs were electrochemically active toward the reduction of molecular oxygen and the oxidation of methanol with higher MAs and SAs than the commercial Pt/C standard. In general, the normalized activities show a trend in both MOR and ORR, favoring our porous platinum NP with respect to the commercial standard.

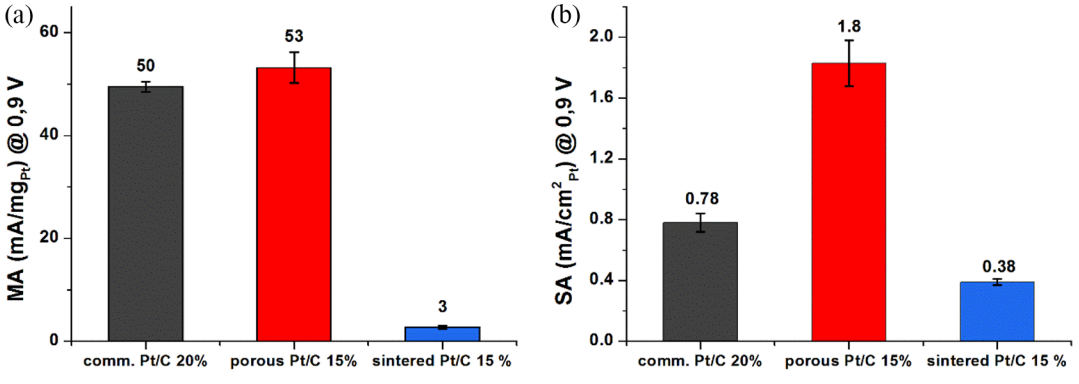

Figure 6. Comparison of MAs (a) and SAs (b) for ORR calculated from values at 0.9 V vs RHE in Figure 5.

https://doi.org/10.1021/acsanm.1c04149
ACS Appl. Nano Mater. 2022, 5, 4710−4720

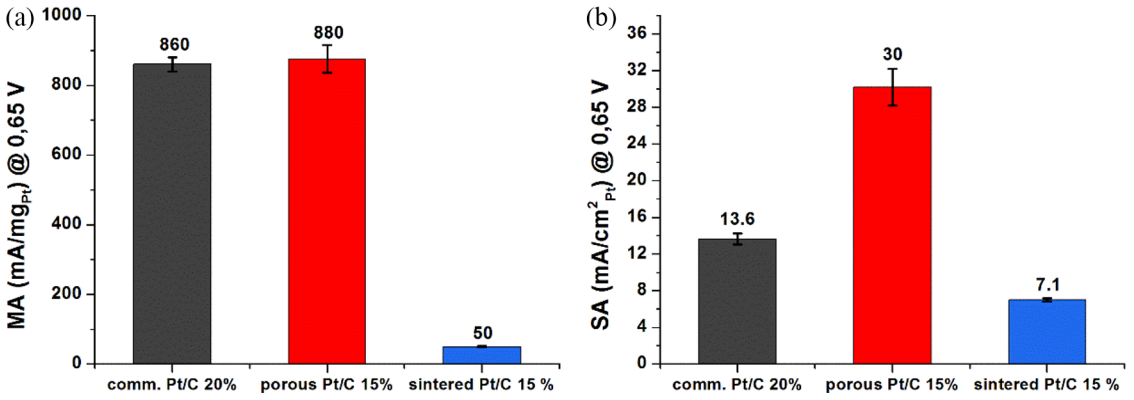

Figure 8. Comparison of MAs (a) and SAs (b) for MOR calculated from values at 0.65 V vs RHE in Figure 7.

■ ASSOCIATED CONTENT

Supporting Information

The Supporting Information is available free of charge at https://pubs.acs.org/doi/10.1021/acsanm.1c04149.

Physisorption data, chemisorption data, powder XRD, dimensional analyses, additional TEM images of the Pt NPs, and IR spectra (PDF)

■ AUTHOR INFORMATION

Corresponding Author

Paolo Fornasiero − *Department of Chemical and Pharmaceutical Sciences, CENMAT, Center of Excellence for Nanostructured Materials, INSTM, UdR Trieste and ICCOM-CNR Trieste Research Unit, University of Trieste, Trieste 34127, Italy;* orcid.org/0000-0003-1082-9157; Email: pfornasiero@units.it

Authors

Mario Daka − *Department of Chemical and Pharmaceutical Sciences, CENMAT, Center of Excellence for Nanostructured Materials, INSTM, UdR Trieste, University of Trieste, Trieste 34127, Italy*

Marcello Ferrara − *Department of Chemical and Pharmaceutical Sciences, CENMAT, Center of Excellence for Nanostructured Materials, INSTM, UdR Trieste, University of Trieste, Trieste 34127, Italy*

Manuela Bevilacqua − *ICCOM-CNR Trieste Research Unit, University of Trieste, Trieste 34127, Italy; ICCOM-CNR, 50019 Sesto Fiorentino, Italy;* orcid.org/0000-0003-4206-104X

Paolo Pengo − *Department of Chemical and Pharmaceutical Sciences, CENMAT, Center of Excellence for Nanostructured Materials, INSTM, UdR Trieste, University of Trieste, Trieste 34127, Italy*

Piu Rajak − *CNR-IOM, 34139 Trieste, Italy*

Regina Ciancio − *CNR-IOM, 34139 Trieste, Italy;* orcid.org/0000-0003-1739-3763

Tiziano Montini − *Department of Chemical and Pharmaceutical Sciences, CENMAT, Center of Excellence for Nanostructured Materials, INSTM, UdR Trieste, University of Trieste, Trieste 34127, Italy;* orcid.org/0000-0001-9515-566X

Lucia Pasquato − *Department of Chemical and Pharmaceutical Sciences, CENMAT, Center of Excellence for Nanostructured Materials, INSTM, UdR Trieste, University of Trieste, Trieste 34127, Italy;* orcid.org/0000-0003-1842-9609

Complete contact information is available at: https://pubs.acs.org/10.1021/acsanm.1c04149

Author Contributions

M.D. conceived and performed the materials syntheses, performed textural characterizations, and wrote the manuscript. M.F. performed and analyzed electrochemical experiments and wrote the manuscript. M.B. supervised electrochemical experiments, discussed the data, and wrote and revised the manuscript. P.P. performed TEM analyses, discussed the data, and wrote and revised the manuscript. P.R. performed HR-TEM and STEM analyses and elaborated the results. R.C. supervised the HR-TEM and STEM analyses. T.M. supervised the XRD characterization, physisorption and chemisorption analyses, contributed to data analysis, and revised the manuscript. L.P. contributed in funding acquisition, discussed the results, and revised the manuscript. P.F. supervised the experiments, discussed the results, and revised the manuscript. All authors have given approval to the final version of the manuscript.

Notes

The authors declare no competing financial interest.

■ ACKNOWLEDGMENTS

This work was supported by the University of Trieste, INSTM, and the Italian Ministry of Education MIUR. M.D., L.P., and P.F. thank the Interreg Strategic project Nano-Region (CUP D99F18000030002) for financial support.

■ REFERENCES

(1) Liu, L.; Corma, A. Metal Catalysts for Heterogeneous Catalysis : From Single Atoms to Nanoclusters and Nanoparticles. *Chem. Rev.* **2018**, *118*, 4981−5079.

(2) Guntern, Y. T.; Okatenko, V.; Pankhurst, J.; Varandili, S. B.; Iyengar, P.; Koolen, C.; Stoian, D.; Vavra, J.; Buonsanti, R. Colloidal Nanocrystals as Electrocatalysts with Tunable Activity and Selectivity. *ACS Catal.* **2021**, *11*, 1248−1295.

(3) Evans, E. R.; Bugga, P.; Asthana, V.; Drezek, R. Metallic Nanoparticles for Cancer Immunotherapy. *Mater. Today* **2018**, *21*, 673−685.

(4) Cao-Milán, R.; Liz-Marzán, L. M. Gold Nanoparticle Conjugates: Recent Advances toward Clinical Applications. *Expert Opin. Drug Delivery* **2014**, *11*, 741−752.

(5) Jain, P. K.; Huang, X.; El-Sayed, I. H.; El-Sayed, M. A. Noble Metals on the Nanoscale: Optical and Photothermal Properties and

Some Applications in Imaging, Sensing, Biology, and Medicine. *Acc. Chem. Res.* **2008**, *41*, 1578−1586.
(6) de Marchi, S.; Núñez-Sánchez, S.; Bodelón, G.; Pérez-Juste, J.; Pastoriza-Santos, I. Pd Nanoparticles as a Plasmonic Material: Synthesis, Optical Properties and Applications. *Nanoscale* **2020**, *12*, 23424−23443.
(7) Zheng, G.; He, J.; Kumar, V.; Wang, S.; Pastoriza-Santos, I.; Pérez-Juste, J.; Liz-Marzán, L. M.; Wong, K. Y. Discrete Metal Nanoparticles with Plasmonic Chirality. *Chem. Soc. Rev.* **2021**, *50*, 3738−3754.
(8) van Muylde, J.; de Zoubov, N. Electrochemical Properties of the Platinum Metals. *Platinum Met. Rev.* **1959**, *3*, 100−106.
(9) Labinger, J. A. Platinum-Catalyzed C−H Functionalization. *Chem. Rev.* **2017**, *117*, 8483−8496.
(10) Sabyrov, K.; Jiang, J.; Yaghi, O. M.; Somorjai, G. A. Hydroisomerization of N-Hexane Using Acidified Metal-Organic Framework and Platinum Nanoparticles. *J. Am. Chem. Soc.* **2017**, *139*, 12382−12385.
(11) Sakai, K.; Ozawa, H. Homogeneous Catalysis of Platinum(II) Complexes in Photochemical Hydrogen Production from Water. *Coord. Chem. Rev.* **2007**, *251*, 2753−2766.
(12) Meemken, F.; Baiker, A. Recent Progress in Heterogeneous Asymmetric Hydrogenation of C=O and C=C Bonds on Supported Noble Metal Catalysts. *Chem. Rev.* **2017**, *117*, 11522−11569.
(13) Liu, K.; Wang, A.; Zhang, T. Recent Advances in Preferential Oxidation of Co Reaction over Platinum Group Metal Catalysts. *ACS Catal.* **2012**, *2*, 1165−1178.
(14) Holton, O. T.; Stevenson, J. W. The Role of Platinum in Proton Exchange Membrane Fuel Cells. *Platinum Met. Rev.* **2013**, *57*, 259−271.
(15) Cargnello, M.; Doan-Nguyen, V. V. T.; Gordon, T. R.; Diaz, R. E.; Stach, E. A.; Gorte, R. J.; Fornasiero, P.; Murray, C. B. Control of Metal Nanocrystal Size Reveals Metal-Support Interface Role for Ceria Catalysts. *Science* **2013**, *341*, 771−773.
(16) Kang, Y.; Li, M.; Cai, Y.; Cargnello, M.; Diaz, R. E.; Gordon, T. R.; Wieder, N. L.; Adzic, R. R.; Gorte, R. J.; Stach, E. A.; Murray, C. B. Heterogeneous Catalysts Need Not Be so "Heterogeneous:" Monodisperse Pt Nanocrystals by Combining Shape-Controlled Synthesis and Purification by Colloidal Recrystallization. *J. Am. Chem. Soc.* **2013**, *135*, 2741−2747.
(17) Kim, H.; Yoo, T. Y.; Bootharaju, M. S.; Kim, J. H.; Chung, D. Y.; Hyeon, T. Noble Metal-Based Multimetallic Nanoparticles for Electrocatalytic Applications. *Adv. Sci.* **2022**, *9*, 1−36.
(18) Meher, S. K.; Cargnello, M.; Troiani, H.; Montini, T.; Rao, G. R.; Fornasiero, P. Alcohol Induced Ultra-Fine Dispersion of Pt on Tuned Morphologies of CeO_2 for CO Oxidation. *Appl. Catal., B* **2013**, *130*−*131*, 121−131.
(19) Lopez, N.; Janssens, T. V. W.; Clausen, B. S.; Xu, Y.; Mavrikakis, M.; Bligaard, T.; Nørskov, J. K. On the Origin of the Catalytic Activity of Gold Nanoparticles for Low-Temperature CO Oxidation. *J. Catal.* **2004**, *223*, 232−235.
(20) Xie, C.; Yan, D.; Li, H.; Du, S.; Chen, W.; Wang, Y.; Zou, Y.; Chen, R.; Wang, S. Defect Chemistry in Heterogeneous Catalysis : Recognition , Understanding , and Utilization. *ACS Catal.* **2020**, *10*, 11082−11098.
(21) Shi, R.; Zhao, Y.; Waterhouse, G. I. N.; Zhang, S.; Zhang, T. Defect Engineering in Photocatalytic Nitrogen Fixation. *ACS Catal.* **2019**, 9739−9750.
(22) Valério Neto, E. S.; Almeida, C. V. S.; Russell, A. E.; Salazar-Banda, G. R.; Eguiluz, K. I. B. Realising the Activity Benefits of Pt Preferential (111) Surfaces for Ethanol Oxidation in a Nanowire Electrocatalyst. *Electrochim. Acta* **2020**, *348*, 1−11.
(23) Schmidt, E.; Vargas, A.; Mallat, T.; Baiker, A. Shape-Selective Enantioselective Hydrogenation on Pt Nanoparticles. *J. Am. Chem. Soc.* **2009**, *131*, 12358−12367.
(24) Bratlie, K. M.; Lee, H.; Komvopoulos, K.; Yang, P.; Somorjai, G. A. Platinum Nanoparticle Shape Effects on Benzene Hydrogenation Selectivity. *Nano Lett.* **2007**, *7*, 3097−3101.
(25) Bennett, D. A.; Cargnello, M.; Diroll, B. T.; Murray, C. B.; Vohs, J. M. Shape-Dependence of the Thermal and Photochemical Reactions of Methanol on Nanocrystalline Anatase TiO2. *Surf. Sci.* **2016**, *654*, 1−7.
(26) Xie, S.; Choi, S.; Xia, X.; Xia, Y. Catalysis on Faceted Noble-Metal Nanocrystals : Both Shape and Size Matter. *Curr. Opin. Chem. Eng.* **2013**, *2*, 142−150.
(27) Kucernak, A.; Jiang, J. Mesoporous Platinum as a Catalyst for Oxygen Electroreduction and Methanol Electrooxidation. *Chem. Eng. J.* **2003**, *93*, 81−90.
(28) Peng, Z.; Yang, H. Synthesis and Oxygen Reduction Electrocatalytic Property of Pt-on-Pd. *J. Am. Chem. Soc.* **2009**, *131*, 7542−7543.
(29) Yu, W.; Batchelor-mcauley, C.; Compton, R. G. Porosity Controls the Catalytic Activity of Platinum Nanoparticles. *Phys. Chem. Chem. Phys.* **2019**, *21*, 20415−20421.
(30) Mohanty, A.; Garg, N.; Jin, R. Zuschriften A Universal Approach to the Synthesis of Noble Metal Nanodendrites and Their Catalytic Properties **. *Am. Ethnol.* **2010**, *122*, 5082−5086.
(31) Wang, L.; Imura, M.; Yamauchi, Y. Tailored Design of Architecturally Controlled Pt Nanoparticles with Huge Surface Areas toward Superior Unsupported Pt Electrocatalysts. *ACS Appl. Mater. Interfaces* **2012**, *4*, 6−10.
(32) Hansen, T. W.; Delariva, A. T.; Challa, S. R.; Datye, A. K. Sintering of Catalytic Nanoparticles : Particle Migration or Ostwald Ripening ? *Acc. Chem. Res.* **2013**, *46*, 1720−1730.
(33) Shin, H. J.; Ryoo, R.; Liu, Z.; Terasaki, O. Template Synthesis of Asymmetrically Mesostructured Platinum Networks. *J. Am. Chem. Soc.* **2001**, *123*, 1246−1247.
(34) Koo, J. H.; Kumar, A.; Lee, S.; Jin, X.; Jeong, H.; Kim, J.; Lee, I. S. Pore-Engineered Silica Nanoreactors for Chemical Interaction-Guided Confined Synthesis of Porous Platinum Nanodendrites. *Chem. Mater.* **2018**, *30*, 3010−3018.
(35) Han, Y.-J.; Kim, J. M.; Stucky, G. D. Preparation of Noble Metal Nanowires Using Hexagonal Mesoporous Silica SBA-15. *Chem. Mater.* **2000**, *12*, 2068−2069.
(36) Proc, J. R.; London, R. S.; Attard, G. S.; Bartlett, P. N.; Coleman, N. R. B.; Elliott, J. M.; Owen, J. R.; Wang, J. H. Mesoporous Platinum Films from Lyotropic Liquid Crystalline Phases. *Science* **1997**, *278*, 13−840.
(37) Warren, S. C.; Messina, L. C.; Slaughter, L. S.; Kamperman, M.; Zhou, Q.; Gruner, S. M.; Disalvo, F. J.; Wiesner, U. Ordered Mesoporous Materials from Metal Nanoparticle − Block Copolymer Self-Assembly. *Science* **2008**, *320*, 1748−1752.
(38) Lu, S.; Eid, K.; Li, W.; Cao, X.; Pan, Y.; Guo, J.; Wang, L.; Wang, H.; Gu, H. Gaseous NH3 Confers Porous Pt Nanodendrites Assisted by Halides. *Sci. Rep.* **2016**, *6*, 1−11.
(39) Mourdikoudis, S.; Chirea, M.; Altantzis, T.; Pastoriza-Santos, I.; Pérez-Juste, J.; Silva, F.; Bals, S.; Liz-Marzán, L. M. Dimethylformamide-Mediated Synthesis of Water-Soluble Platinum Nanodendrites for Ethanol Oxidation Electrocatalysis. *Nanoscale* **2013**, *5*, 4776−4784.
(40) Erlebacher, J.; Aziz, M. J.; Karma, A.; Dimitrov, N.; Sieradzki, K. Evolution of Nanoporosity in Dealloying. *Nature* **2001**, *410*, 450−453.
(41) Shui, J. L.; Chen, C.; Li, J. C. M. Evolution of Nanoporous Pt-Fe Alloy Nanowires by Dealloying and Their Catalytic Property for Oxygen Reduction Reaction. *Adv. Funct. Mater.* **2011**, *21*, 3357−3362.
(42) Akbar, S.; Elliott, J. M.; Squires; Anwar, A. Optimum Conditions for Electrochemical Deposition of 3-D Mesoporous Platinum Framework. *J. Nanopart. Res.* **2020**, *22*, 1.
(43) Zhang, W.; Yang, J.; Lu, X. Tailoring Galvanic Replacement Reaction for the Preparation of Pt/Ag Bimetallic Hollow Nanostructures with Controlled Number of Voids. *ACS Nano* **2012**, *6*, 7397−7405.
(44) Ye, F.; Hu, W.; Zhang, T.; Yang, J.; Ding, Y. Enhanced Electrocatalytic Activity of Pt-Nanostructures Prepared by Electrodeposition Using Poly(Vinyl Pyrrolidone) as a Shape-Control Agent. *Electrochim. Acta* **2012**, *83*, 383−386.

https://doi.org/10.1021/acsanm.1c04149
ACS Appl. Nano Mater. 2022, 5, 4710−4720

(45) Ullah, M. H.; Chung, W. S.; Kim, I.; Ha, C. S. PH-Selective Synthesis of Monodisperse Nanoparticles and 30 Dendritic Nanoclusters of CTAB-Stabilized Platinum for Electrocatalytic O2 Reduction. *Small* **2006**, *2*, 870−873.
(46) Wang, S.; Kuai, L.; Huang, Y.; Yu, X.; Liu, Y.; Li, W.; Chen, L.; Geng, B. A Highly Efficient, Clean-Surface, Porous Platinum Electrocatalyst and the Inhibition Effect of Surfactants on Catalytic Activity. *Chem. − Eur. J.* **2013**, *19*, 240−248.
(47) Lim, B.; Lu, X.; Jiang, M.; Camargo, P. H. C.; Cho, E. C.; Lee, E. P.; Xia, Y. Facile Synthesis of Highly Faceted Multioctahedral Pt Nanocrystals through Controlled Overgrowth. *Nano Lett.* **2008**, *8*, 4043−4047.
(48) Lacroix, L. M.; Gatel, C.; Arenal, R.; Garcia, C.; Lachaize, S.; Blon, T.; Warot-Fonrose, B.; Snoeck, E.; Chaudret, B.; Viau, G. Tuning Complex Shapes in Platinum Nanoparticles: From Cubic Dendrites to Fivefold Stars. *Angew. Chem., Int. Ed.* **2012**, *51*, 4690−4694.
(49) Arán-Ais, R. M.; Vidal-Iglesias, F. J.; Solla-Gullón, J.; Herrero, E.; Feliu, J. M. Electrochemical Characterization of Clean Shape-Controlled Pt Nanoparticles Prepared in Presence of Oleylamine/Oleic Acid. *Electroanalysis* **2015**, *27*, 945−956.
(50) Khan, M. D.; Opallo, M.; Revaprasadu, N. Colloidal Synthesis of Metal Chalcogenide Nanomaterials from Metal-Organic Precursors and Capping Ligand Effect on Electrocatalytic Performance: Progress, Challenges and Future Perspectives. *Dalton Trans.* **2021**, *50*, 11347−11359.
(51) Chen, R.; Yang, C.; Cai, W.; Wang, H. Y.; Miao, J.; Zhang, L.; Chen, S.; Liu, B. Use of Platinum as the Counter Electrode to Study the Activity of Nonprecious Metal Catalysts for the Hydrogen Evolution Reaction. *ACS Energy Lett.* **2017**, *2*, 1070−1075.
(52) Shinozaki, K.; Zack, J. W.; Pylypenko, S.; Pivovar, B. S.; Kocha, S. S. Oxygen Reduction Reaction Measurements on Platinum Electrocatalysts Utilizing Rotating Disk Electrode Technique. *J. Electrochem. Soc.* **2015**, *162*, F1384−F1396.
(53) Shinozaki, K.; Zack, J. W.; Richards, R. M.; Pivovar, B. S.; Kocha, S. S. Oxygen Reduction Reaction Measurements on Platinum Electrocatalysts Utilizing Rotating Disk Electrode Technique. *J. Electrochem. Soc.* **2015**, *162*, F1144−F1158.
(54) Rudi, S.; Cui, C.; Gan, L.; Strasser, P. Comparative Study of the Electrocatalytically Active Surface Areas (ECSAs) of Pt Alloy Nanoparticles Evaluated by Hupd and CO-Stripping Voltammetry. *Electrocatalysis* **2014**, *5*, 408−418.
(55) Rodríguez, P.; Solla-Gullón, J.; Vidal-Iglesias, F. J.; Herrero, E.; Aldaz, A.; Feliu, J. M. Determination of (111) Ordered Domains on Platinum Electrodes by Irreversible Adsorption of Bismuth. *Anal. Chem.* **2005**, *77*, 5317−5323.
(56) Rodriguez, P.; Herrero, E.; Solla-Gullón, J.; Vidal-Iglesias, F. J.; Aldaz, A.; Feliu, J. M. Electrochemical Characterization of Irreversibly Adsorbed Germanium on Platinum Stepped Surfaces Vicinal to Pt(1 0 0). *Electrochim. Acta* **2005**, *50*, 3111−3121.
(57) Solla-Gullón, J.; Rodríguez, P.; Herrero, E.; Aldaz, A.; Feliu, J. M. Surface Characterization of Platinum Electrodes. *Phys. Chem. Chem. Phys.* **2008**, *10*, 1359−1373.
(58) Solla-Gullón, J.; Montiel, V.; Aldaz, A.; Clavilier, J. Electrochemical Characterisation of Platinum Nanoparticles Prepared by Microemulsion: How to Clean Them without Loss of Crystalline Surface Structure. *J. Electroanal. Chem.* **2000**, *491*, 69−77.
(59) Teng, X.; Liang, X.; Maksimuk, S.; Yang, H. Synthesis of Porous Platinum Nanoparticles. *Small* **2006**, *2*, 249−253.
(60) Pasricha, R.; Bala, T.; Biradar, A. V.; Umbarkar, S.; Sastry, M. Synthesis of Catalytically Active Porous Platinum Nanoparticles by Transmetallation Reaction and Proposition of the Mechanism. *Small* **2009**, *5*, 1467−1473.
(61) Jiang, B.; Li, C.; Malgras, V.; Imura, M.; Tominaka, S.; Yamauchi, Y. Mesoporous Pt Nanospheres with Designed Pore Surface as Highly Active Electrocatalyst. *Chem. Sci.* **2016**, *7*, 1575−1581.
(62) Kang, Y.; Ye, X.; Murray, C. B. Size- and Shape-Selective Synthesis of Metal Nanocrystals and Nanowires Using CO as a Reducing Agent. *Angew. Chem., Int. Ed.* **2010**, *49*, 6156−6159.
(63) Mourdikoudis, S.; Liz-Marzán, L. M. Oleylamine in Nanoparticle Synthesis. *Chem. Mater.* **2013**, 1465−1476.
(64) Teng, X.; Yang, H. Synthesis of Platinum Multipods: An Induced Anisotropic Growth. *Nano Lett.* **2005**, *5*, 885−891.
(65) Chen, J.; Herricks, T.; Geissler, M.; Xia, Y. Single-Crystal Nanowires of Platinum Can Be Synthesized by Controlling the Reaction Rate of a Polyol Process. *J. Am. Chem. Soc.* **2004**, *126*, 10854−10855.
(66) Song, Y.; Yang, Y.; Medforth, C. J.; Pereira, E.; Singh, A. K.; Xu, H.; Jiang, Y.; Brinker, C. J.; van Swol, F.; Shelnutt, J. A. Controlled Synthesis of 2-D and 3-D Dendritic Platinum Nanostructures. *J. Am. Chem. Soc.* **2004**, *126*, 635−645.
(67) Gao, Q.; Gao, M. R.; Liu, J. W.; Chen, M. Y.; Cui, C. H.; Li, H. H.; Yu, S. H. One-Pot Synthesis of Branched Palladium Nanodendrites with Superior Electrocatalytic Performance. *Nanoscale* **2013**, *5*, 3202−3207.
(68) Mourdikoudis, S.; Montes-García, V.; Rodal-Cedeira, S.; Winckelmans, N.; Pérez-Juste, I.; Wu, H.; Bals, S.; Pérez-Juste, J.; Pastoriza-Santos, I. Highly Porous Palladium Nanodendrites: Wet-Chemical Synthesis, Electron Tomography and Catalytic Activity. *Dalton Trans.* **2019**, *48*, 3758−3767.
(69) Wen, X.; Lerch, S.; Wang, Z.; Aboudiab, B.; Tehrani-Bagha, A. R.; Olsson, E.; Moth-Poulsen, K. Synthesis of Palladium Nanodendrites Using a Mixture of Cationic and Anionic Surfactants. *Langmuir* **2020**, *36*, 1745−1753.
(70) Wang, L.; Yamauchi, Y. Facile Synthesis of Three-Dimensional Dendritic Platinum Nanoelectrocatalyst. *Chem. Mater.* **2009**, *21*, 3562−3569.
(71) Wang, L.; Wang, H.; Nemoto, Y.; Yamauchi, Y. Rapid and Efficient Synthesis of Platinum Nanodendrites with High Surface Area by Chemical Reduction with Formic Acid. *Chem. Mater.* **2010**, *22*, 2835−2841.
(72) Lu, X.; Tuan, H.-Y.; Korgel, B. A.; Xia, Y. Facile Synthesis of Gold Nanoparticles with Narrow Size Distribution by Using AuCl or AuBr as the Precursor. *Chem. − Eur. J.* **2008**, *14*, 1584−1591.
(73) Angerstein-Kozlowska, H.; Conway, B. E.; Sharp, W. B. A. The real condition of electrochemically oxidized platinum surfaces: Part I. Resolution of component processes. *J. Electroanal. Chem. Interfacial Electrochem.* **1973**, *43*, 9−36.
(74) Diaz-Morales, O.; Hersbach, T. J. P.; Badan, C.; Garcia, A. C.; Koper, M. T. M. Hydrogen Adsorption on Nano-Structured Platinum Electrodes. *Faraday Discuss.* **2018**, *210*, 301−315.
(75) Bertin, E.; Garbarino, S.; Guay, D.; Solla-Gullón, J.; Vidal-Iglesias, F. J.; Feliu, J. M. Electrodeposited Platinum Thin Films with Preferential (100) Orientation: Characterization and Electrocatalytic Properties for Ammonia and Formic Acid Oxidation. *J. Power Sources* **2013**, *225*, 323−329.
(76) Xia, B. Y.; Wu, H. B.; Wang, X.; Lou, X. W. Highly Concave Platinum Nanoframes with High-Index Facets and Enhanced Electrocatalytic Properties. *Angew. Chem., Int. Ed.* **2013**, *52*, 12337−12340.
(77) Lai, J.; Niu, W.; Qi, W.; Zhao, J.; Li, S.; Gao, W.; Luque, R.; Xu, G. A Platinum Highly Concave Cube with One Leg on Each Vertex as an Advanced Nanocatalyst for Electrocatalytic Applications. *ChemCatChem* **2015**, *7*, 1064−1069.

https://doi.org/10.1021/acsanm.1c04149
ACS Appl. Nano Mater. 2022, 5, 4710−4720